AGU PUBLICATIONS

Geophysical Research Letters

RESEARCH LETTER
10.1002/2016GL071163

Key Points:
- New detailed GPS velocity field in Bhutan showing lateral variations of interseismic coupling
- Decoupled upper ramp of the Main Himalayan Thrust in eastern Bhutan
- Potential first evidence of transient events on the Main Himalayan Thrust

Supporting Information:
- Supporting Information S1

Correspondence to:
A. Marechal,
marechal@gm.univ-montp2.fr

Citation:
Marechal, A., et al. (2016), Evidence of interseismic coupling variations along the Bhutan Himalayan arc from new GPS data, *Geophys. Res. Lett.*, *43*, doi:10.1002/2016GL071163.

Received 9 SEP 2016
Accepted 5 DEC 2016
Accepted article online 9 DEC 2016

Evidence of interseismic coupling variations along the Bhutan Himalayan arc from new GPS data

Anais Marechal[1], Stephane Mazzotti[1], Rodolphe Cattin[1], Gael Cazes[2], Philippe Vernant[1], Dowchu Drukpa[3], Kinzang Thinley[4], Alizia Tarayoun[1], Romain Le Roux-Mallouf[1], Bal Bahadur Thapa[4], Phuntsho Pelgay[3], Jampel Gyeltshen[3], Erik Doerflinger[1], and Stéphanie Gautier[1]

[1]Geosciences Montpellier, UMR5243, Université de Montpellier, Montpellier, France, [2]School of Earth and Environmental Sciences, University of Wollongong, Wollongong, New South Wales, Australia, [3]Seismology and Geophysics Division, Department of Geology and Mines, Ministry of Economic Affairs, Thimphu, Bhutan, [4]National Land Commission, Royal Government of Bhutan, Thimphu, Bhutan

Abstract Although the first-order pattern of present-day deformation is relatively well resolved across the Himalayas, irregular data coverage limits detailed analyses of spatial variations of interseismic coupling. We provide the first GPS velocity field for the Bhutan Himalaya. Combined with published data, these observations show strong east-west variations in coupling between central and eastern Bhutan. In contrast with previous estimations of first-order uniform interseismic coupling along the Himalayan arc, we identify significant lateral variations: In western and central Bhutan, the fully coupled segment is 135–155 km wide with an abrupt downdip transition, whereas in eastern Bhutan the fully coupled segment is 100–120 km wide and is limited updip and downdip by partially creeping segments. This is the first observation of decoupling on the upper ramp along the Himalayan arc, with important implications for large earthquake surface rupture and seismic hazard.

1. Introduction

In the Himalayas, as in all active tectonic regions, strain budget on the main seismogenic faults during large earthquakes and over interseismic periods is a key element to improve seismic hazard assessment. The first-order present-day crustal deformation along the Himalayan arc is now relatively well constrained from leveling data [*Jackson and Bilham*, 1994], interferometric synthetic aperture radar observations [*Grandin et al.,* 2012], and GPS measurements [e.g., *Bettinelli et al.,* 2006; *Jade et al.,* 2011; *Vernant et al.,* 2014]. Altogether, these observations show that nearly all of the present-day convergence is accommodated along the Main Himalayan Thrust (MHT), which reaches the surface at the Main Boundary Thrust (MBT) and Main Frontal Thrust (MFT). However, data coverage remains irregular, and areas such as Bhutan Himalaya are poorly constrained. This lack of data results in significant limitations in the interseismic strain analysis. Although the MHT is considered as fully locked along its entire length without any aseismic barrier [*Stevens and Avouac*, 2015], small-scale decoupled or aseismic region might exist in regions such as Bhutan, where the geodetic data are, up to now, limited to a few stations [*Vernant et al.,* 2014].

Here we provide the first detailed GPS velocity solution for the region of Bhutan Himalaya, consisting in (1) north-south profiles composed of nineteen campaign stations installed and surveyed in western, central, and eastern Bhutan since 2003, (2) nine new campaign stations deployed in central and eastern Bhutan in 2012, and (3) eight permanent stations distributed across the country and operating since 2011 (except for two older stations that operated from 2003 to 2008). Combined with published data, these new GPS observations are used to improve the assessments of interseismic coupling along the MHT and of the first-order geometry of the unlocked portions of the fault at depth. After a brief presentation of the GPS data, we describe the modeling approach and discuss its results and implications in terms of east-west lateral variations of present-day interseismic strain buildup.

2. Methodology

2.1. GPS Data

We extend the GPS data published for the Kingdom of Bhutan by *Vernant et al.* [2014] with (1) nine new campaign sites installed in 2013 and 2014 in central and eastern Bhutan, surveyed between 2013 and

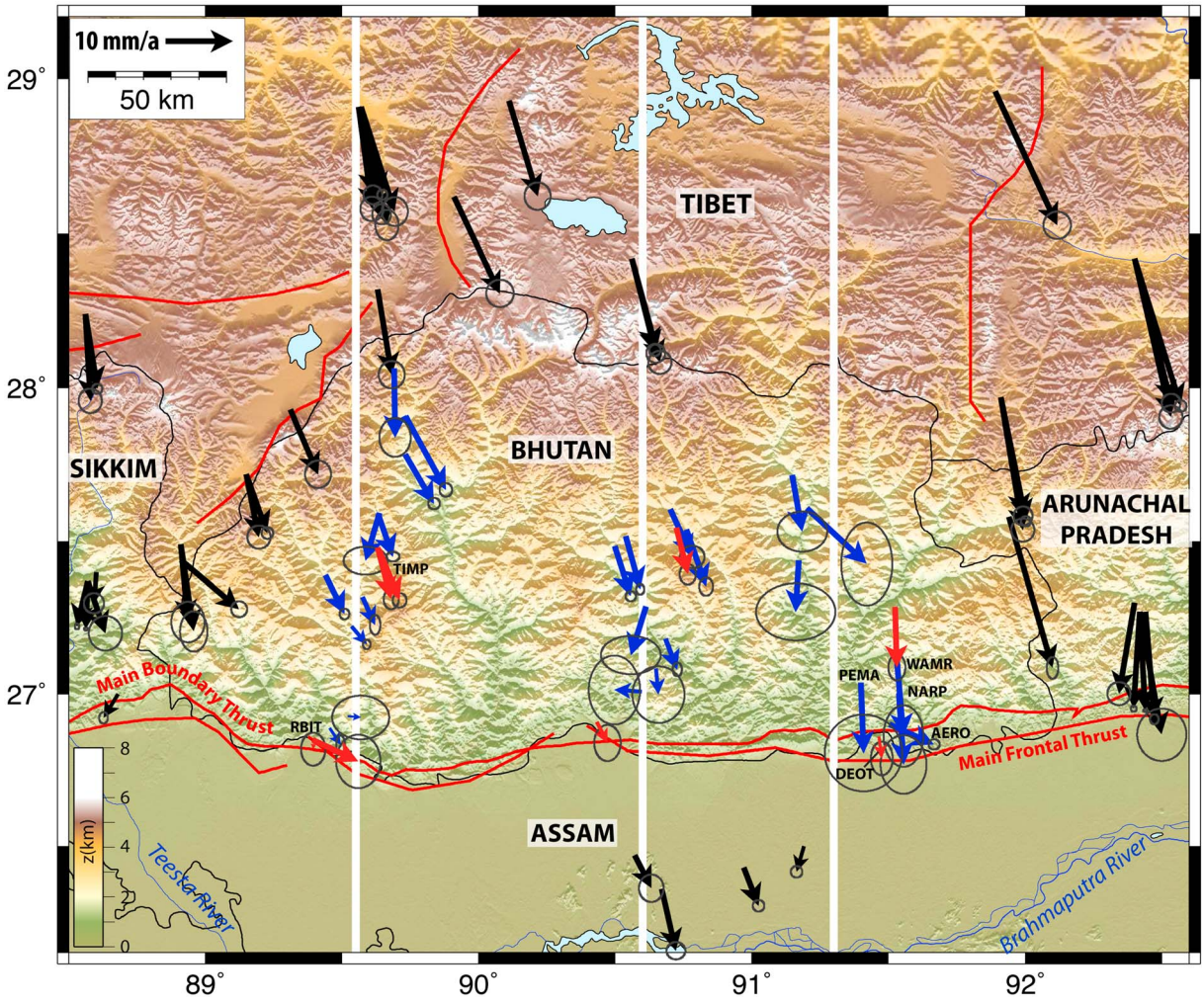

Figure 1. New GPS velocity field for Bhutan Himalaya relative to stable India (as defined by *Ader et al.* [2012]). Blue and red vectors show campaign and permanent GPS data from this study, respectively. Black vectors are from *Banerjee et al.* [2008], *Bettinelli et al.* [2006], *Gahalaut et al.* [2013], *Gan et al.* [2007], *Jade* [2004], *Jade et al.* [2007], *Jade et al.* [2014], *Liang et al.* [2013], *Mahesh et al.* [2012], *Mukul et al.* [2010], *Tang et al.* [2010], and *Vernant et al.* [2014]. Ellipses indicate 1σ confidence regions.

2016, (2) four campaign sites installed and surveyed in 2003 and reoccupied between 2013 and 2016, and (3) six permanent sites installed in 2011 and 2012 by the National Land Commission (NLC) of Bhutan. The full network comprises 28 campaign stations and 8 permanent sites (Figure 1). The continuous site data span 2003–2008 (TIMP and RBIT) and 2011–2016 (new NLC sites). Data for the campaign sites range between 2003 and 2016, with a minimum of two surveys over 2 years for the newest sites (Table S1 in the supporting information). Campaign and permanent sites are instrumented with geodetic-grade receivers and antennas, and campaign sites were surveyed at the same period (March-April) for at least 24 h (commonly over 48 h) for each campaign.

GPS daily positions in the International GNSS Service reference frame IGb08 are calculated with the CSRS-Precise Point Positioning v1.5 software [*Héroux and Kouba*, 2001] using the approach described in *Marechal et al.* [2015]. Velocities are estimated by a least squares inversion weighted by the position formal uncertainties. The inverted model comprises a linear term (velocity) and, for the permanent stations, an annual sinusoid to account for seasonal effects, mostly related to the load variations of the Brahmaputra River alluvial plain. The final velocities (Table S1) are expressed relative to stable India using the India/International Terrestrial Reference Frame rotation defined by *Ader et al.* [2012]. We do not apply corrections for transient events such as coseismic displacements, which are not significant in Bhutan [*Vernant et al.*, 2014].

Velocity uncertainties are calculated using the formulation of *Mao et al.* [1999] assuming that the campaign and permanent data are characterized by a "white + flicker" colored noise model. Long gaps in the Bhutan permanent time series preclude a robust noise analysis of the local data. Thus, we use analyses of permanent data with similar PPP processing in western Europe and North America [*Marechal et al.,* 2015; *Nguyen et al.,* 2016] to define average noise model parameters. We derive scaling coefficients between the time series root-mean-square dispersion and white and flicker noise amplitudes for these data sets, which are then applied to the Bhutan permanent and campaign data. This approach puts an emphasis on both the length and number of data points of the time series, with mean horizontal velocity standard errors of 3.5–4.5 mm/yr for data spanning 2–3 years versus 1.0–1.5 mm/yr for longer data sets (Table S1).

2.2. Modeling Approach

The most conventional approach used to reproduce interseismic GPS velocities and assess interseismic coupling is the back slip dislocation model [*Savage*, 1983], which considers virtual normal faulting along the seismogenic portion of the MHT [e.g., *Stevens and Avouac,* 2015]. However, the back slip formulation is only rigorously correct for a purely planar fault or a fully locked fault [*Vergne et al.,* 2001]. Hence, although back slip models can provide a good fit to geodetic data, it cannot be used to assess potential partial coupling along the Bhutanese MHT, which is well known for its flat and ramp geometry [e.g., *Long et al.,* 2011; *Coutand et al.,* 2014; *Le Roux-Mallouf et al.,* 2015].

Here we favor the use of a dislocation model of buried reverse faults associated with aseismic slip, allowing us to assess simultaneously the convergence rate, potential partial coupling, and the geometry of the unlocked portions of the MHT [e.g., *Vergne et al.,* 2001; *Kanda and Simons,* 2010]. Because the three-dimensional geometry of the MHT remains poorly constrained in our study region, we use a two-dimensional approach along three north-south profiles, orthogonal to the regional MFT direction, in western, central, and eastern Bhutan (Figure 1). We project the GPS velocities along the profiles and only consider the component of coupling parallel to the profile directions, thus neglecting the small oblique component of the regional convergence.

For each profile, the geometry of the MHT is defined by the coordinates of six breakpoints that allow to model a complex ramp-flat system and to take into account slip rate variations with depth (Figure 2a and Table S2). Assuming that the depth of the MHT increases northward, these coordinates are treated as dependent parameters. Furthermore, available geological and geophysical data along our study profiles are used as a priori knowledge of these coordinates [*Coutand et al.,* 2014; *Le Roux-Mallouf et al.,* 2015]. This includes (1) the location of the emergence of the MHT at the surface with a maximum dip angle of 50° [*Long et al.,* 2011], (2) a subhorizontal section at a depth of 10–15 km [*Bhattacharyya and Mitra*, 2009; *Acton et al.,* 2011; *Long et al.,* 2011; *Tobgay et al.,* 2012], (3) a maximum dip angle of 30° for crustal ramp(s) as imaged by seismic experiments in Garhwal, Nepal, and Sikkim [*Nábělek et al.,* 2009; *Acton et al.,* 2011; *Caldwell et al.,* 2013], and (4) a depth of ~40 km of the southernmost point imaged beneath southern Tibet from the INDEPTH experiment (International Deep Profiling of Tibet and the Himalaya) [*Hauck et al.,* 1998]. We also assume a convergence of 15 to 25 mm/yr for the three profiles, consistent with the estimate across western Bhutan from GPS observations [*Vernant et al.,* 2014].

In order to solve the nonlinear equations linking surface displacements with fault slip rate and geometry at depth [e.g., *Okada*, 1985], data inversion is performed using a pseudorandom walk through the parameter space, which consists of 14 parameters including the slip rates for the five fault segments (u_1 to u_5) as well as the depth and distance along the profile of the six breakpoints (Figure 2a and Table S2). Following *Mosegaard and Tarantola* [1995], a Markov Chain Monte Carlo technique is used to generate a large collection of 10^8 models with stochastic sampling that depends on the posterior probability of the model likelihood. This pseudorandom walk is controlled by the following rules for the transition from model m_i to model m_j:

1. If $L(m_j) \geq L(m_i)$ then accept the proposed transition from i to j,
2. If $L(m_j) < L(m_i)$ then the proposed transition from i to j has a probability $L(m_j)/L(m_i)$,

where $L(m_i)$ and $L(m_j)$ are the likelihood of the old and the new models, respectively. We define the likelihood function L of a model m as

$$L(m) = \exp\left(-\frac{1}{n}\sum_{i=1}^{n}\left(\frac{\mathrm{Ucalc}_i - \mathrm{Uobs}_i}{\sigma_i}\right)^2\right),$$

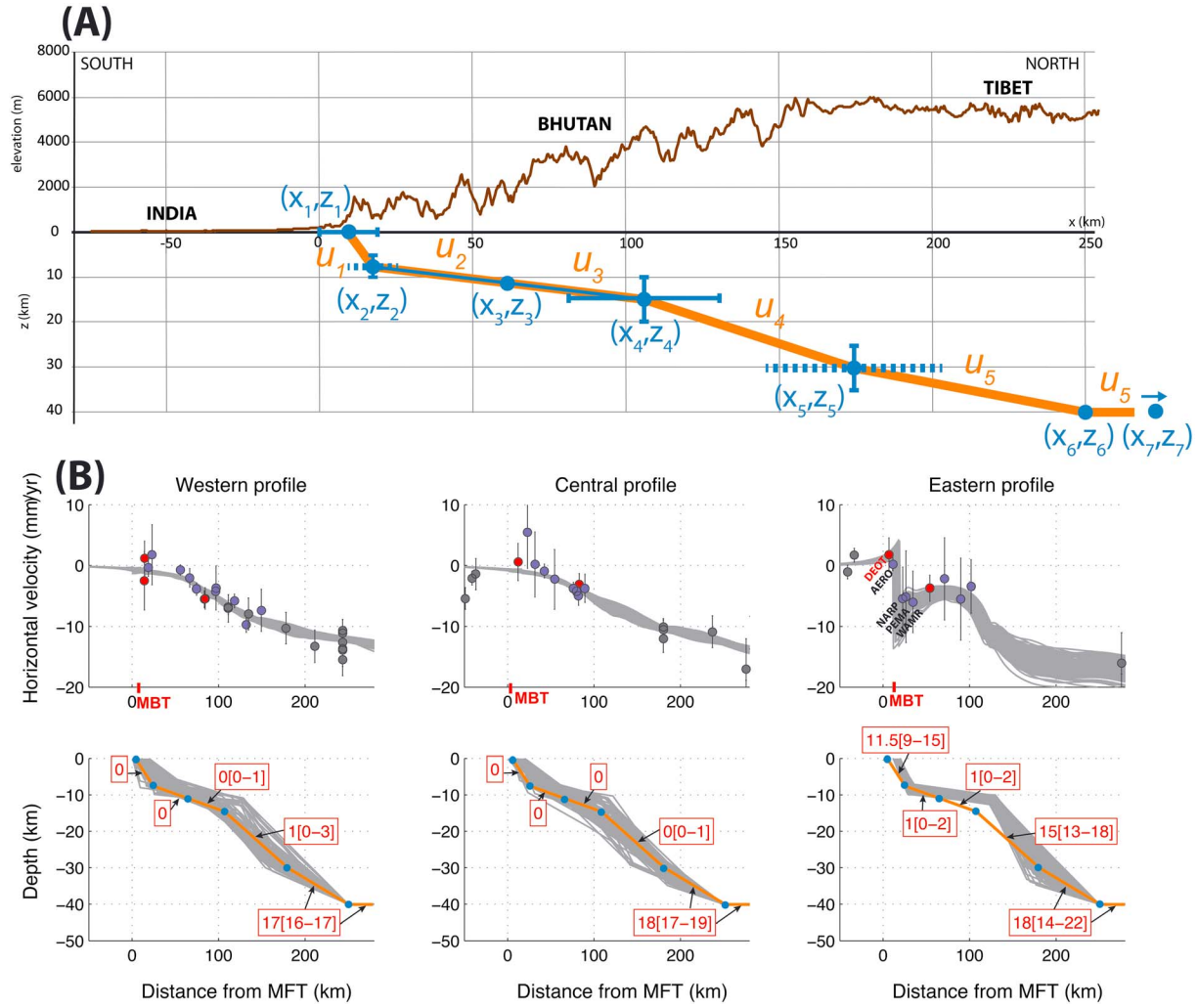

Figure 2. Model geometry and fault slip rates. (a) Geometry used in the inversion. Orange: a priori geometry. The ranges of the fault breakpoints (blue dots and segments) and allowed slip rates are detailed in Table S2. Dashed blue segments represent the angle constraint for points 2 and 5. Note that vertical scales are different for the topography and at depth. (b) Horizontal velocity profiles across western, central, and eastern Bhutan (see Figure 1 for locations). Gray lines are associated with the 100 best models. (top) GPS (circles, cf. Figure 1 for color legend) and calculated (lines) velocities. Note that GPS horizontal velocities are projected along the profile. (bottom) Obtained fault geometry (gray lines) and overthrusting slip rates (in red rectangles). Numbers in bracket corresponds to the slip rate uncertainties. Orange lines show the a priori model.

where n is the number of data points, $U\text{obs}_i$ is the observed GPS velocity and σ_i is the velocity uncertainty, and $U\text{calc}_i$ is the velocity calculated from the analytical solution given by *Singh and Rani* [1993] assuming a two-dimensional dip-slip fault embedded in a homogeneous half-space.

We only use the horizontal components of the GPS velocity vectors, projected along the profile direction, due to the limited availability of good-quality vertical velocities (see section 4 for a comparison of the models with vertical data). The posterior probability of each model parameter is obtained from the final collection of the sampled models (Figures 2, 3, and S1). In the following, the results of the inversion are presented in terms of highest density probability value (preferred value) and full width at half maximum (uncertainty).

3. Results

Our results indicate a present-day far-field convergence rate ~ 16.5–17.5 mm/a, without significant lateral variations along the Bhutan Himalaya arc (Figures 2b and 3), consistent with estimates of 17.6 ± 0.9 mm/a [*Stevens and Avouac*, 2015] and 15.5 ± 1.5 mm/a [*Vernant et al.*, 2014]. In contrast with this uniform convergence rate, we highlight lateral variations of interseismic slip pattern at depth (cf. Figures 2b and 3).

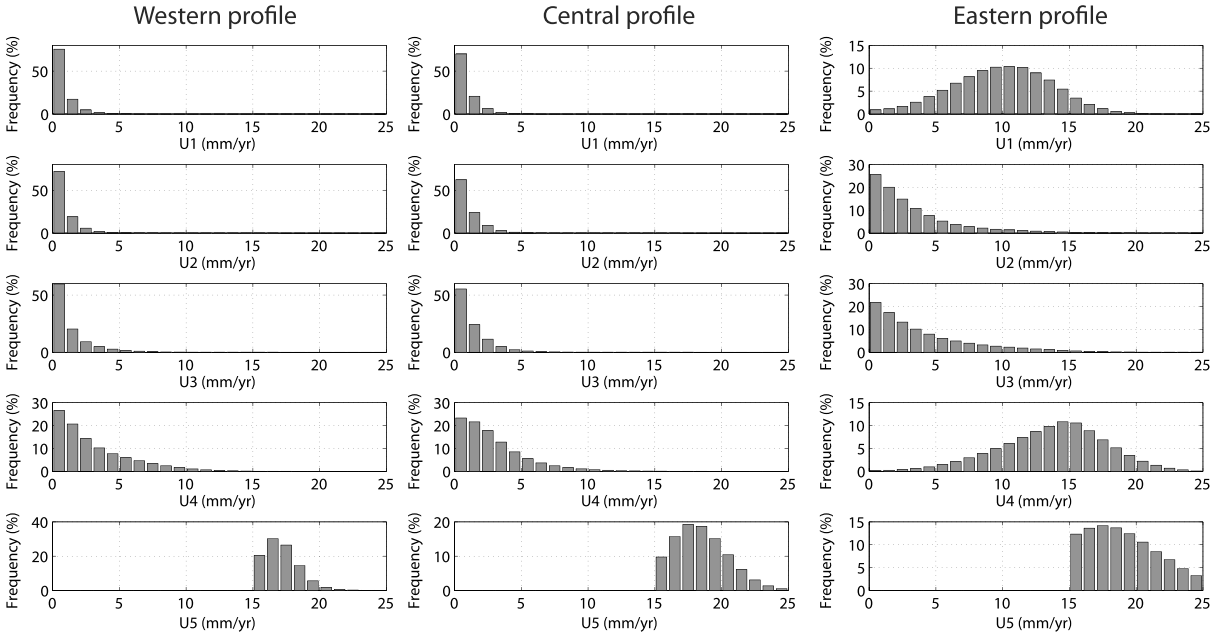

Figure 3. Slip rate posterior distributions on fault segments. u_1 to u_5 are the slip rates along the fault (from south to north, cf. Figure 2a) on the western, central, and eastern profiles.

1. Along the western and central Bhutan profiles, slip pattern is mostly bimodal, with an abrupt decrease on the crustal ramp from full convergence on the lower segment of the ramp (u_5) to near-zero slip rate on the upper segments (u_1 to u_4). The dense GPS coverage along these profiles (less than 30 km between sites) allows a good definition of this abrupt transition, as shown by the tight constraints on its location ($\pm$10 km) and on the slip rates of the various segments (Table S2).
2. In contrast with the western and central profiles, the interseismic slip pattern on the eastern profile shows a smoother transition on the deepest ramp with u_4 = 10–18 mm/a (illustrating the capacity of our analysis to resolve a gradual downdip transition). However, because of the lack of GPS coverage between 100 and 260 km north of the MFT, the precise location of this transition is poorly resolved (breakpoint 5, Figure S1d).
3. Whereas the slip rate on the flat segment of the MHT is similar for the three profiles (u_2 and u_3~ 0 mm/a), the shallow upper ramp of the eastern profile exhibits a higher slip rate with u_1 = 5.5–14.5 mm/a. This aseismic slip on the upper ramp is well constrained owing to very good data coverage within the $\pm$50 km of the MFT: Specifically, the three sites located north of the MBT (NARP, PEMA, and WAMR, above segment u_1) have the same velocity and present an abrupt change of ~6 mm/a compare to the sites directly south of the MBT (DEOT and AERO, see Figure 2b).

In our modeling approach, a fault segment with a null velocity is similar to no fault and its geometry cannot be constrained by the inversion. However, we can obtain information on the MHT geometry for the creeping segments, albeit with variable sensitivity on the different parameters (i.e., spread of the 100 best models, Figure 2b). This sensitivity can be assessed from the posterior probability distributions that show near-uniform probabilities for segments with near-zero slip rates in contrast with sharp probability clusters for faster creeping segments (cf. Figure S1). On this basis, new constraints on the MHT geometry can be derived for the creeping segments (Table S2).

1. The deepest and northernmost limit of the fully coupled section is located 135–155 km north of the MFT on the western and central profiles (breakpoint 5—Figures S1b and S1c) but only 120–130 km for the eastern profile (breakpoint 4—Figure S1d).
2. The deep flat-ramp transition is located 120–130 km north of the MFT in eastern Bhutan (breakpoint 4—Figure S1d).
3. The depth of the flat segment is constrained to 9–12 km in eastern Bhutan (breakpoints 2, 3, and 4—Figure S1d).

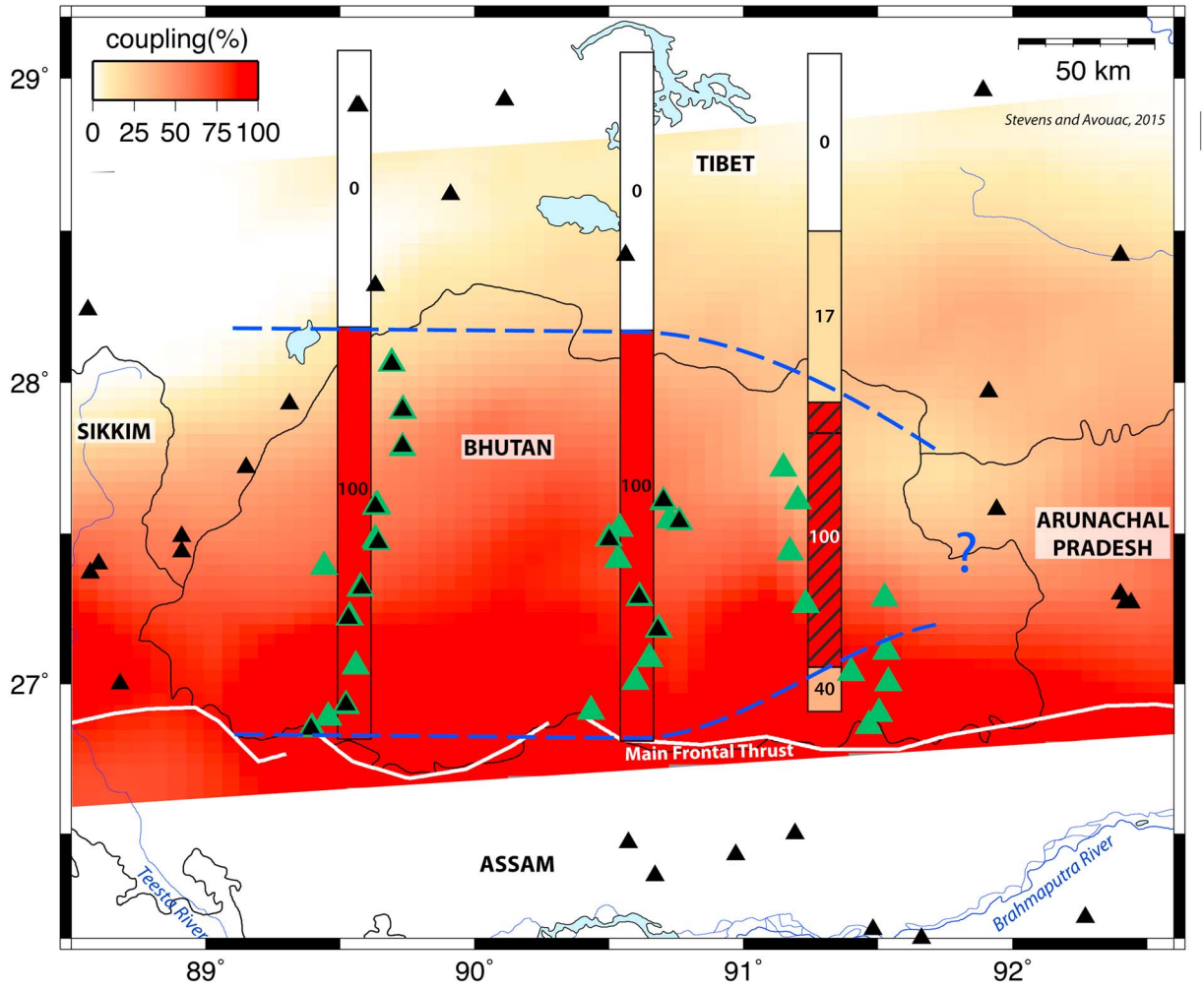

Figure 4. Interseismic coupling of the Main Himalayan Thrust in Bhutan. Rectangles show our estimates of interseismic coupling for the different fault segments. The hatched segment represents the flat part of the MHT constrained by the inversion. The colored base map represents the estimates of *Stevens and Avouac* [2015]. Dashed blue lines show the possible limits of the fully coupled zone. Green triangles show the locations of our new GPS stations. Black triangles are GPS stations used in the solution of *Stevens and Avouac* [2015].

4. On the eastern profile, active faulting takes place on the MBT, i.e., 13–20 km north of the MFT (breakpoint 1—Figure S1d). On both sides and nearby the surface expression of the upper fault segment, the GPS coverage is dense: DEOT and AERO, located between the MFT and MBT, have similar velocities to those south of the MFT, and we measure an abrupt change of ~ 6 mm/yr across the MBT (Figure 2b). These results indicate that the MBT in eastern Bhutan is currently active and that it accommodates part of the convergence by aseismic creep.

4. Discussion

In order to compare our results with other studies, we describe the interseismic state of the MHT in terms of coupling, defined as the ratio between the fault interseismic slip rate and the present-day far-field convergence rate ($u_5 = 17 \pm 2$ mm/a). On the basis of a smooth back slip model, *Stevens and Avouac* [2015] conclude that a frontal ~ 100 km large portion of the MHT is fully locked in Bhutan (coupling $>$ 50%). They argue for an abrupt transition to a decoupled segment along the downdip ramp, although their smoothed large-scale coupling map does not clearly resolve this transition pattern (Figure 4). The addition of new GPS data in western and central Bhutan allows us to better define this transition and its location. Our slip rate posterior distribution (Figure 3) shows that the interseismic coupling decreases northward from 100% to 0% along the deep ramp

segment, about 145 km north of the MFT in western and central Bhutan (Figure 4 and Table S2). Our results also indicate a significant change in the coupling pattern between central and eastern Bhutan, with a smoother transition (17% of coupling on the deeper ramp) and a slightly less wide coupled zone (100–120 km versus 135–155 km) along the eastern profile. We show for the first time in the Himalayas that the upper ramp is partially decoupled (40% (17–70%) of coupling), suggesting that the long-term convergence may not be fully expressed in large earthquakes in this particular region.

The current resolution of the vertical GPS velocities remains too low to provide significant constraints to our slip rate analysis. However, a first-order comparison of uplift rates from our campaign stations (with other 10 years of data) versus other geological indicators shows the potential importance of these data sets for short-and long-term uplift constraints. In western Bhutan, our vertical GPS velocities suggest a peak of 2–3.5 mm/a about 100 km north of the MFT (Figure S2), whereas Holocene denudation rates indicate a sharp peak of ~2 mm/a 130–150 km north of the MFT with near-zero rates between 40 and 110 km [*Le Roux-Mallouf et al.,* 2015; *Portenga et al*., 2014; *Adams et al.,* 2016]. This difference in patterns likely reflects the difference in measurement time scales: GPS data cover a decadal interseismic period and are mostly sensitive to the coupled-decoupled transition; denudation data are representative of several thousand years over several seismic cycles and are primarily sensitive to the fault geometry. A few additional years of campaign GPS data combined with longer-term denudation and incision data may thus provide important constraints on the geometry and seismic behavior of the MHT.

Our analysis of new GPS data in Bhutan provide three major constraints to the interseismic state of the MHT: (1) An abrupt downdip termination of the fully coupled segment, about 145 km north of the MFT in western and central Bhutan; (2) a less wide fully coupled segment in eastern Bhutan (~110 km), with a partially unlocked deeper crustal ramp; (3) in this eastern region, the MBT is creeping and is part of the active thrusting front. These observations raise questions regarding the seismic and interseismic behavior of the MHT. We infer creep on the eastern Bhutan MBT on the basis of velocity measurements over 3 years (2013–2016); hence, we cannot resolve whether this represents long-term creep or could potentially correspond to a transient slip episode on the upper part of the MHT, which would contribute to release part of the interseismic stress buildup. Similarly, our observation of partial creep on the MBT suggests that an event similar to the recent 2015 Gorkha earthquake occurring on the MHT could potentially not reach the surface in eastern Bhutan.

Acknowledgments
This project is funded by the French Agence Nationale de la Recherche (ANR-13-BS06-0006-01). We are grateful to the Department of Geology and Mines, M. Chokila and the National Land Commission of Bhutan for their major contributions to the field campaigns. The 2013–2016 surveys benefited from the support of the French RESIF-GPSMob Research Infrastructure (http://www.resif.fr). The discussion greatly benefited from talks with J.-P. Avouac whom we warmly thank. The manuscript has been greatly improved by helpful suggestions by Editor A.V. Newman and two anonymous reviewers. Data availability: Campaign GPS data for the 2003 survey are from R. Bilham project (NSF Cooperative Agreement EAR-0735156) and are available on the UNAVCO archive (https://www.unavco.org/data/gps-gnss/gps-gnss.html). Campaign GPS data for the 2013–2016 surveys are available on the RESIF-GPSMob archive (https://gpsmob.resif.fr) and by request to the authors for other periods. Permanent GPS data are available by request to the National Land Commission of Bhutan. GPS data processing was done with CSRS-PPP v1.5 provided by Natural Resources Canada (https://webapp.geod.nrcan.gc.ca/geod/tools-outils/ppp.php), using the International GNSS Service precise products (http://www.igs.org/products). GPS time series analysis was done with R software (https://www.r-project.org) with codes available by request to the authors. The slip rate and geometry inversion software is available by request to the authors.

References

Acton, C. E., K. Priestley, S. Mitra, and V. K. Gaur (2011), Crustal structure of the Darjeeling—Sikkim Himalaya and southern Tibet, *Geophys. J. Int.*, *184*(2), 829–852.

Adams, B. A., K. X. Whipple, K. V. Hodges, and A. M. Heimsath (2016), In situ development of high-elevation, low-relief landscapes via duplex deformation in the Eastern Himalayan hinterland, Bhutan, *J. Geophys. Res. Earth Surf.*, *121*, 294–319, doi:10.1002/2015JF003508.

Ader, T., et al. (2012), Convergence rate across the Nepal Himalaya and interseismic coupling on the Main Himalayan Thrust: Implications for seismic hazard, *J. Geophys. Res.*, *117*, B04403, doi:10.1029/2011JB009071.

Banerjee, P., R. Bürgmann, B. Nagarajan, and E. Apel (2008), Intraplate deformation of the Indian subcontinent, *Geophys. Res. Lett.*, *35*, L18301, doi:10.1029/2008GL035468.

Bettinelli, P., J. P. Avouac, M. Flouzat, F. Jouanne, L. Bollinger, P. Willis, and G. R. Chitrakar (2006), Plate motion of India and interseismic strain in the Nepal Himalaya from GPS and DORIS measurements, *J. Geod.*, *80*(8–11), 567–589.

Bhattacharyya, K., and G. Mitra (2009), A new kinematic evolutionary model for the growth of a duplex—An example from the Rangit duplex, Sikkim Himalaya, India, *Gondwana Res.*, *16*(3), 697–715.

Caldwell, W. B., S. L. Klemperer, J. F. Lawrence, S. S. Rai, and Ashish (2013), Characterizing the Main Himalayan Thrust in the Garhwal Himalaya, India with receiver function CCP stacking, *Earth Planet. Sci. Lett.*, *367*, 15–27, doi:10.1016/j.epsl.2013.02.009.

Coutand, I., D. M. Whipp Jr., D. Grujic, M. Bernet, M. G. Fellin, B. Bookhagen, K. R. Landry, S. K. Ghalley, and C. Duncan (2014), Geometry and kinematics of the Main Himalayan Thrust and Neogene crustal exhumation in the Bhutanese Himalaya derived from inversion of multi-thermochronologic data, *J. Geophys. Res. Solid Earth*, *119*, 1446–1481, doi:10.1002/2013JB010891.

Gahalaut, V. K., et al. (2013), Aseismic plate boundary in the Indo-Burmese wedge, northwest Sunda Arc, *Geology*, *41*(2), 235–238.

Gan, W., P. Zhang, Z.-K. Shen, Z. Niu, M. Wang, Y. Wan, D. Zhou, and J. Cheng (2007), Present-day crustal motion within the Tibetan Plateau inferred from GPS measurements, *J. Geophys. Res.*, *112*, B08416, doi:10.1029/2005JB004120.

Grandin, R., M. P. Doin, L. Bollinger, B. Pinel-Puysségur, G. Ducret, R. Jolivet, and S. N. Sapkota (2012), Long-term growth of the Himalaya inferred from interseismic InSAR measurement, *Geology*, *40*(12), 1059–1062.

Hauck, M. L., K. D. Nelson, L. D. Brown, W. Zhao, and A. R. Ross (1998), Crustal structure of the Himalayan orogen at ~90 east longitude from Project INDEPTH deep reflection profiles, *Tectonics*, *17*, 481–500, doi:10.1029/98TC01314.

Héroux, P., and J. Kouba (2001), GPS precise point positioning using IGS orbit products, *Phys. Chem. Earth, Part A*, *26*(6), 573–578.

Jackson, M., and R. Bilham (1994), Constraints on Himalayan deformation inferred from vertical velocity fields in Nepal and Tibet, *J. Geophys. Res.*, *99*, 13–897, doi:10.1029/94JB00714.

Jade, S. (2004), Estimates of plate velocity and crustal deformation in the Indian subcontinent using GPS geodesy, *Curr. Sci.*, *86*, 1443–1448.

Jade, S., et al. (2007), Estimates of interseismic deformation in northeast India from GPS measurements, *Earth Planet. Sci. Lett.*, *263*(3), 221–234.

Jade, S., H. R. Rao, M. S. M. Vijayan, V. K. Gaur, B. C. Bhatt, K. Kumar, S. Jaganathan, M. B. Ananda, and P. D. Kumar (2011), GPS-derived deformation rates in northwestern Himalaya and Ladakh, *Int. J. Earth Sci.*, *100*(6), 1293–1301.

Jade, S., et al. (2014), Contemporary deformation in the Kashmir–Himachal, Garhwal and Kumaon Himalaya: Significant insights from 1995–2008 GPS time series, *J. Geod.*, *88*(6), 539–557.

Kanda, R. V. S., and M. Simons (2010), An elastic plate model for interseismic deformation in subduction zones, *J. Geophys. Res.*, *115*, B03405, doi:10.1029/2009JB006611.

Le Roux-Mallouf, R., et al. (2015), Evidence for a wide and gently dipping Main Himalayan Thrust in western Bhutan, *Geophys. Res. Lett.*, *42*, 3257–3265, doi:10.1002/2015GL063767.

Liang, S., W. Gan, C. Shen, G. Xiao, J. Liu, W. Chen, X. Ding, and D. Zhou (2013), Three-dimensional velocity field of present-day crustal motion of the Tibetan Plateau derived from GPS measurements, *J. Geophys. Res. Solid Earth*, *118*, 5722–5732, doi:10.1002/2013JB010503.

Long, S., N. McQuarrie, T. Tobgay, and D. Grujic (2011), Geometry and crustal shortening of the Himalayan fold-thrust belt, eastern and central Bhutan, *Geol. Soc. Am. Bull.*, *123*(7/8), 1427–1447, doi:10.1130/B30203.1.

Mahesh, P., et al. (2012), Rigid Indian plate: Constraints from GPS measurements, *Gondwana Res.*, *22*(3), 1068–1072.

Mao, A., C. G. Harrison, and T. H. Dixon (1999), Noise in GPS coordinate time series, *J. Geophys. Res.*, *104*, 2797–2816, doi:10.1029/1998JB900033.

Marechal, A., S. Mazzotti, J. L. Elliott, J. T. Freymueller, and M. Schmidt (2015), Indentor-corner tectonics in the Yakutat-St. Elias collision constrained by GPS, *J. Geophys. Res. Solid Earth*, *120*, 3897–3908, doi:10.1002/2014JB011842.

Mosegaard, K., and A. Tarantola (1995), Monte Carlo sampling of solutions to inverse problems, *J. Geophys. Res.*, *100*, 12,431–12,447, doi:10.1029/94JB03097.

Mukul, M., S. Jade, A. Bhattacharyya, and K. Bhusan (2010), Crustal shortening in convergent orogens: Insights from Global Positioning System (GPS) measurements in northeast India, *J. Geol. Soc. India*, *75*(1), 302–312, doi:10.1007/s12594-010-0017-9.

Nábělek, J., G. Hetényi, J. Vergne, S. Sapkota, B. Kafle, M. Jiang, H. Su, J. Chen, B. S. Huang, and the Hi-CLIMB Team (2009), Underplating in the Himalaya-Tibet collision zone revealed by the Hi-CLIMB experiment, *Science*, *325*(5946), 1371–1374, doi:10.1126/science.1167719.

Nguyen, H. N., P. Vernant, S. Mazzotti, G. Khazaradze, and E. Asensio (2016), 3D GPS velocity field and its implications on the present-day post-orogenic deformation of the Western Alps and Pyrenees, *Solid Earth*, *7*, 1349–1363.

Okada, Y. (1985), Surface deformation due to shear and tensile faults in a half-space, *Bull. Seismol. Soc. Am.*, *75*(4), 1135–1154.

Portenga, E. W., P. R. Bierman, C. Duncan, L. B. Corbett, N. M. Kehrwald, and D. H. Rood (2014), Erosion rates of the Bhutanese Himalaya determined using in situ-produced ^{10}Be, *Geomorphology*, *233*, 112–126.

Savage, J. C. (1983), A dislocation model of strain accumulation and release at a subduction zone, *J. Geophys. Res.*, *88*, 4984–4996, doi:10.1029/JB088iB06p04984.

Singh, S. J., and S. Rani (1993), Crustal deformation associated with two-dimensional thrust faulting, *J. Phys. Earth*, *41*, 87–101.

Stevens, V. L., and J. P. Avouac (2015), Interseismic coupling on the main Himalayan thrust, *Geophys. Res. Lett.*, *42*, 5828–5837, doi:10.1002/2015GL064845.

Tang, L., C. Li, J. Zhang, X. Shl, and P. Wei (2010), Precise monitoring technique for regional surface deformation using GPS/CORS observation, *Bull. Surv. Mapp.*, *5*, 6–9.

Tobgay, T., N. McQuarrie, S. Long, M. J. Kohn, and S. L. Corrie (2012), The age and rate of displacement along the Main Central Thrust in the western Bhutan Himalaya, *Earth Planet. Sci. Lett.*, *319*, 146–158.

Vergne, J., R. Cattin, and J. P. Avouac (2001), On the use of dislocations to model interseismic strain and stress build-up at intracontinental thrust faults, *Geophys. J. Int.*, *147*, 155–162.

Vernant, P., R. Bilham, W. Szeliga, D. Drupka, S. Kalita, A. K. Bhattacharyya, V. K. Gaur, P. Pelgay, R. Cattin, and T. Berthet (2014), Clockwise rotation of the Brahmaputra Valley relative to India: Tectonic convergence in the eastern Himalaya, Naga Hills, and Shillong Plateau, *J. Geophys. Res. Solid Earth*, *119*, 6558–6571, doi:10.1002/2014JB011196.

Geophysical Research Letters

Supporting Information for

Evidence of interseismic coupling variations along the Bhutan Himalayan arc from new GPS data

Anais Marechal[1], Stephane Mazzotti[1], Rodolphe Cattin[1], Gael Cazes[2], Philippe Vernant[1], Dowchu Drukpa[3], Kinzang Thinley[4], Alizia Tarayoun[1], Romain Le Roux-Mallouf[1], Bal Bahadur Thapa[4], Phuntsho Pelgay[3], Jampel Gyeltshen[3], Erik Doerflinger[1], Stéphanie Gautier[1]

[1] Geosciences Montpellier, UMR5243, Université de Montpellier, Place E. Bataillon, 34 095 Montpellier, France

[2] School of Earth and Environmental Sciences, University of Wollongong, Wollongong, NSW, Australia

[3] Seismology and Geophysics Division, Department of Geology and Mines, Ministry of Economic Affairs, Post Box 173, Thimphu, Bhutan

[4] National Land Commission, Royal Government of Bhutan, Post Box 142, Thimphu, Bhutan

Contents of this file

Introduction

This supporting information contains (1) GPS velocities and (2) inversions results, prior and posterior ranges and likelihood probability distributions of the model parameters (fault segment geometries and slip rates).

Table S1. GPS velocities and associated standard errors (1σ uncertainty) in North, East and Up components. Length: duration of the time series used to calculate the velocities (in year). Nobs: number of surveys for the campaign sites or percentage of days of observations for the time series duration for the permanent sites.

			Velocity relative to stable India (Ader et al., 2012) (mm/a)			Velocity in ITRF2008 (mm/a)			1σ uncertainty (mm/a)				
station	**lat. (°)**	**lon. (°)**	**North**	**East**	**Up**	**North**	**East**	**Up**	**North**	**East**	**Up**	**length (a)**	**Nobs**
AERO	26.90	91.50	-3.0	6.6	-7.2	31.84	46.38	-7.19	0.7	0.8	1.3	12.4	4
AUTS	27.44	91.17	-7.7	-0.5	5.5	27.18	39.02	5.51	3.9	5.5	13.6	2.0	2
BHUM	27.54	90.72	-6.9	1.7	-1.1	27.92	41.05	-1.12	1.4	1.1	1.9	3.5	47.9%
CHUC	27.48	90.50	-7.4	2.4	2.5	27.47	41.65	2.53	0.7	0.7	1.2	12.4	4
DEOT	26.86	91.46	-3.2	0.4	-2.2	31.61	40.18	-2.2	2.3	1.5	2.8	3.5	61.2%
DGON	27.52	90.54	-7.9	2.2	0.3	26.96	41.48	0.34	0.7	0.6	1.4	12.4	3
DODI	27.59	89.63	-6.4	2.2	4.2	28.51	41.19	4.2	0.7	0.9	2.7	12.4	5
GANG	27.22	89.53	-2.7	2.3	0.3	32.18	41.4	0.34	0.7	0.5	1.1	12.4	4
GASA	27.91	89.73	-10.9	6.0	0.1	23.95	44.9	0.07	0.9	0.9	3.1	8.6	3
GEDU	26.93	89.52	-0.2	2.0	-3.6	34.73	41.15	-3.64	3.0	3.9	6.4	3.0	2
GELE	26.91	90.43	-3.1	1.6	-1.8	31.76	41.05	-1.8	2.5	1.8	3.8	3.5	63.6%
GENE	27.32	89.57	-4.2	1.9	-1.0	30.71	40.95	-0.96	1.4	0.7	2.2	12.4	4
JAKR	27.54	90.76	-8.5	2.9	4.2	26.41	42.29	4.19	1.3	1.0	1.2	12.4	4
KABU	27.79	89.73	-7.4	4.3	3.1	27.52	43.25	3.06	0.8	0.8	2.8	12.5	4
KAMJ	26.89	89.45	-2.5	1.6	1.2	32.39	40.83	1.15	1.3	0.6	1.1	12.4	2
KANG	27.29	91.52	-9.1	0.3	-2.2	25.79	39.9	-2.2	1.8	1.2	2.1	4.1	20.9%
KHOS	27.29	90.61	-7.3	-2.3	3.8	27.62	37.12	3.81	2.7	4.1	3.3	3.0	2
KNGA	27.41	90.53	-28.6	2.1	-14.8	6.23	41.4	-14.76	0.9	0.7	0.6	3.0	2
KURJ	27.61	90.70	-7.1	3.3	1.3	27.76	42.56	1.28	1.6	1.7	4.9	12.4	4

LAYA	28.06	89.69	-10.3	0.1	-3.1	24.6	39	-3.12	2.7	2.2	3.3	3.0	2
LHUE	27.72	91.15	-8.4	1.5	-9.9	26.46	40.88	-9.94	2.8	3.4	7.9	3.1	3
MONG	27.26	91.23	-1.7	6.0	-12.3	33.19	45.6	-12.25	2.4	35.4	16.2	3.1	3
NARP	27.00	91.54	-10.7	0.7	20.8	24.18	40.45	20.84	4.0	3.2	5.0	2.0	2
PARO	27.39	89.44	-5.8	2.9	-1.4	29.09	41.88	-1.37	0.7	0.7	1.5	12.4	2
PEMA	27.04	91.40	-10.5	0.4	7.6	24.37	40.08	7.56	5.3	5.4	13.3	2.0	2
PHUN	26.85	89.39	-1.4	0.0	-0.6	33.5	39.18	-0.55	2.3	1.7	3.2	3.6	31.2%
RBIT	26.85	89.39	-3.2	6.8	-16.2	31.73	45.99	-16.21	3.7	3.1	6.1	2.2	75.2%
SAMK	27.01	90.60	0.3	-4.1	14.5	35.14	35.42	14.53	4.8	3.5	11.1	2.0	2
TAMA	27.08	90.65	-3.9	0.4	2.4	30.99	39.82	2.35	3.9	3.6	10.5	2.0	2
TAN2	27.61	91.20	-8.3	8.9	-24.2	26.57	48.36	-24.19	5.7	3.5	14.7	2.0	2
TANG	27.59	89.64	-7.1	-2.1	1.1	27.77	36.92	1.07	1.9	3.0	4.9	12.5	3
THIM	27.48	89.63	-7.7	2.0	-0.2	27.22	41.06	-0.2	1.4	1.0	1.9	4.6	55.8%
TIMP	27.47	89.63	-7.5	3.1	-3.9	27.43	42.12	-3.85	1.0	1.0	2.1	5.2	82.9%
WAMR	27.11	91.53	-11.2	1.0	-588.5	23.66	40.67	-588.53	4.2	2.8	4.6	3.1	2
WONK	27.06	89.56	3.5	14.4	-3.0	38.38	53.55	-3.01	0.1	2.2	0.2	3.0	2
ZHEM	27.18	90.68	-4.6	1.7	0.5	30.25	41.18	0.47	1.0	0.6	2.4	12.4	4

Table S2. Prior and posterior distributions of inversion parameters. Prior constraints (column 2): investigated range of the free parameters used in the inversion. Note that parameters are not independent. Posterior values (columns 3-5): parameter values associated with the most likely model and associated uncertainties (in parenthesis) for the western, central and eastern profiles. Uncertainties are given by the full width at half maximum of the posterior distributions (cf. text). Symbols "-" indicate parameters that are not constrained by the inversion. Cf. Fig. S1b-d for the posterior distributions.

Parameter	**Prior constraints**	**Posterior values**		
number of models	10^8	West	Central	East
x_1 (km)	from 0 to 20	-	-	13 (13-20)
z_1 (km)	0	0	0	0
x_2 (km)	from $x_1 + z_2$ /tan(50°) to $x_1 + z_2$ /tan(10°)	-	-	30 (30-35)
z_2 (km)	from 5 to 10	-	-	9 (9-10)
x_3 (km)	from x_2 to x_4	-	-	115 (100-125)
z_3 (km)	from z_2 to z_4 This point is on the line segment from (x_2,z_2) to (x_4,z_4)	-	-	10 (9-11)
x_4 (km)	from 80 to 130	-	-	125 (120-130)
z_4 (km)	from 10 to 20	-	-	11 (10-12)
x_5 (km)	from $x_4+(z_5-z_4)/\tan(\alpha_{min})$ to $x_4+(z_5-z_4)/\tan(30°)$	145 (135-145)	145 (135-155)	185 (170-205)
z_5 (km)	from 25 to 35 With α_{min} the lowest dip angle between the two line segments [(x_2,z_2); (x_4,z_4)] and [(x_4,z_4); (x_6,z_6)]	26 (25-27)	29 (27-31)	26 (25-28)
x_6 (km)	250	250	250	250
z_6 (km)	40	40	40	40
x_7 (km)	1000	1000	1000	1000
z_7 (km)	40	40	40	40
U_1 (mm/yr)	from 0 to U_4	0	0	10.5 (5.5-14.5)
U_2 (mm/yr)	from 0 to U_4	0	0	0 (0-2)
U_3 (mm/yr)	from 0 to U_4	0	0	0 (0-3)
U_4 (mm/yr)	from 0 to U_5	0 (0-3)	0 (0-3)	14.5 (10-18)
U_5 (mm/yr)	from 15 to 25	16.5 (15-18)	17.5 (15-20)	17.5 (15-22)

Figure S1a. Bivariate frequency histograms showing the prior distribution of the fault breakpoint coordinates. Due to dependencies between parameters, these distributions are not homogeneous, especially for points 2 and 3. The position of point 1 is only given as the x coordinate as the depth z is fixed at 0 km. Cf. Table S2 for constraints on the prior parameter ranges and dependencies.

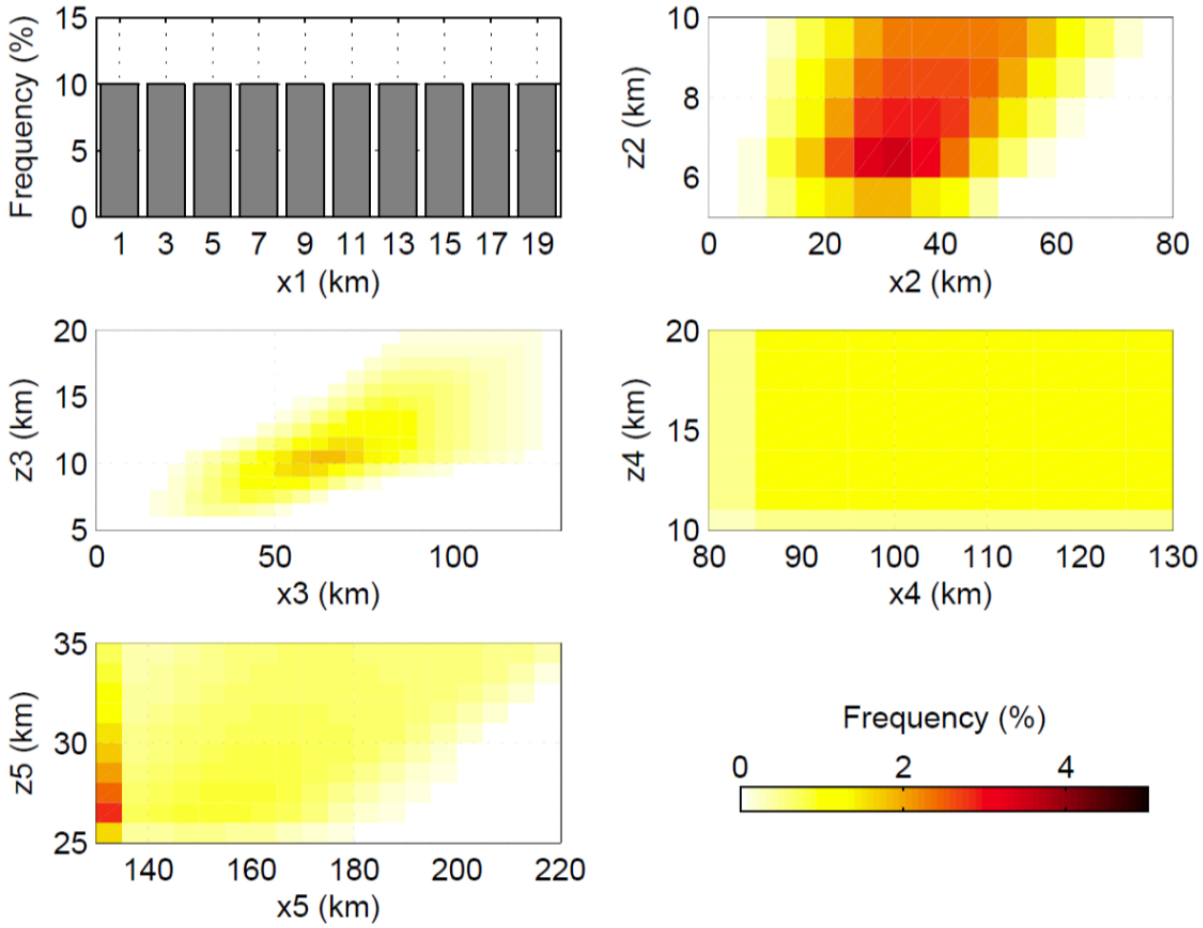

Figure S1b. Fault geometry obtained from inversion of horizontal GPS data for western Bhutan. The bivariate frequency histograms represent the parameter likelihood constrained by GPS data only. In order to correct for prior distribution biases due to parameter dependencies (cf. Fig. S1a), these posterior distributions correspond to the difference between the full frequency histograms obtained by the inversion and the prior histograms.

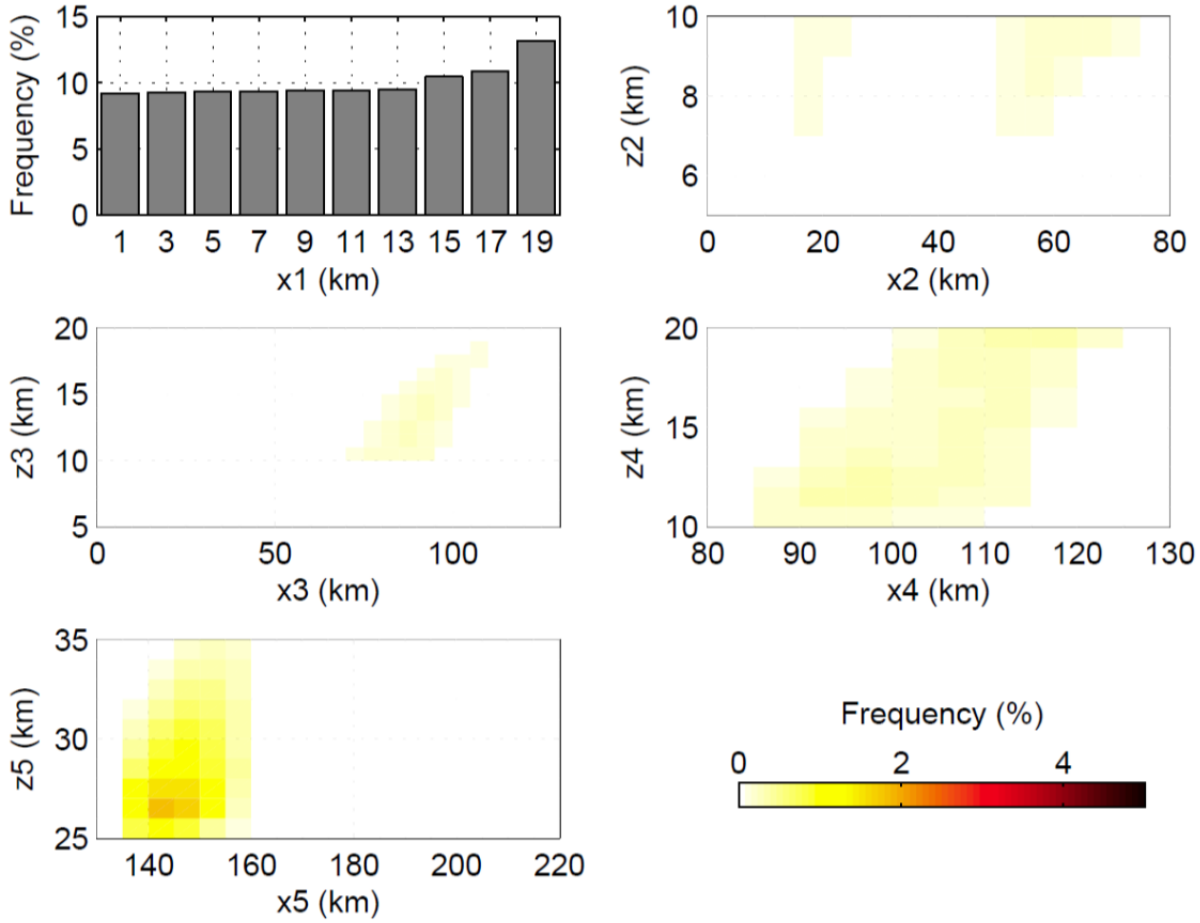

Figure S1c. Same as figure S1b for central Bhutan.

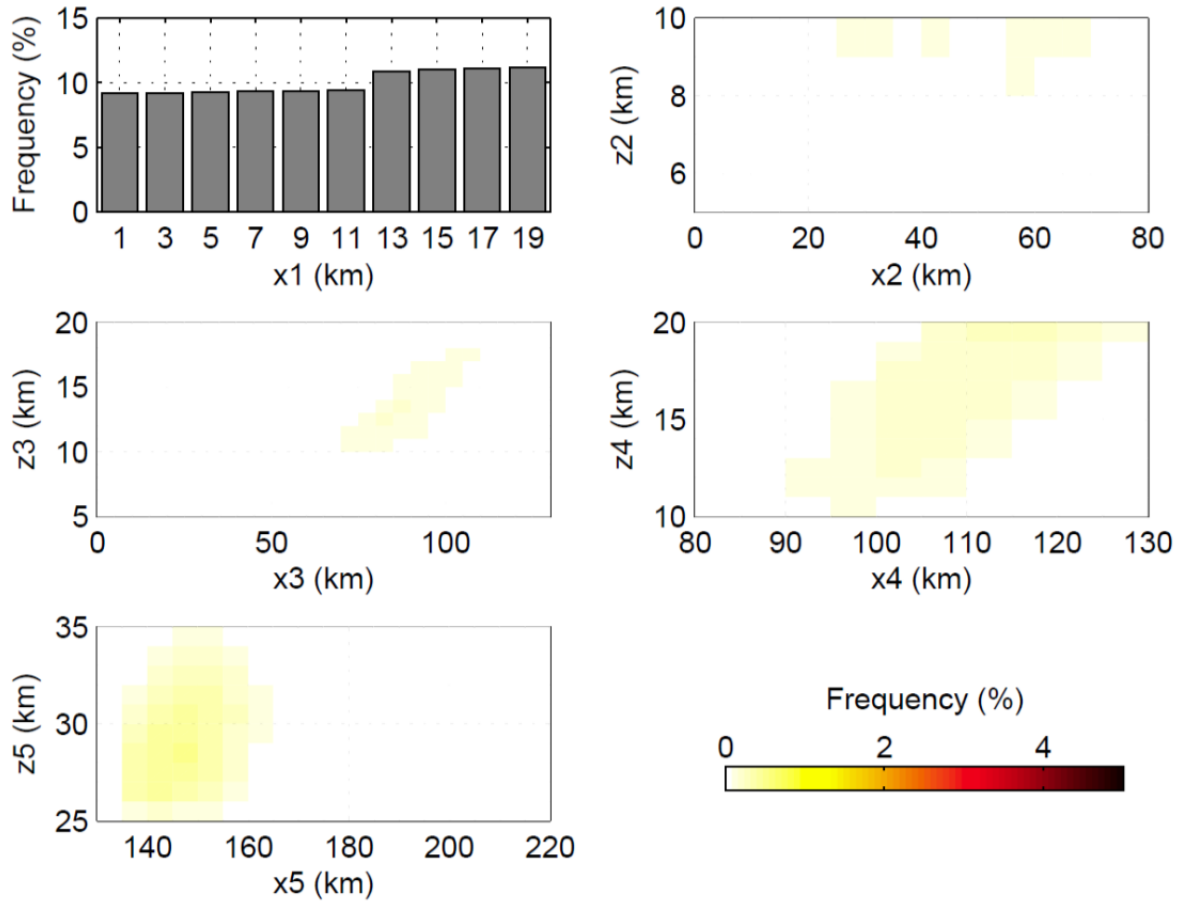

Figure S1d. Same as figure S1b for eastern Bhutan.

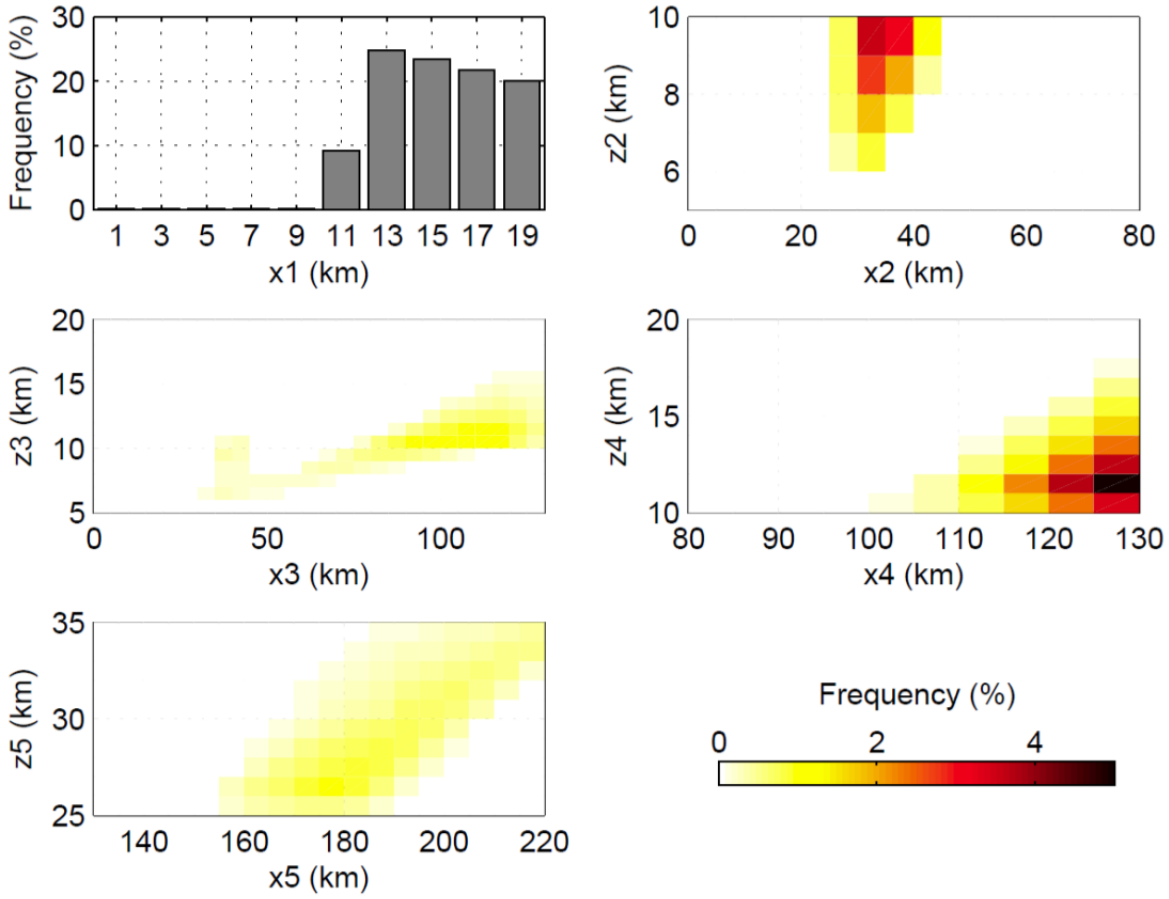

Figure S2. Observed and model-derived vertical velocities in western and central Bhutan. Gray lines are associated with the 100 best models. Blue circles show vertical GPS velocities for campaign stations with over 10 years of data. Green diamonds show the denudation rates derived from cosmogenic nuclides concentration in riverbed sediments (Le Roux-Mallouf *et al.*, 2015); Red squares from Adams et al. (2016); Orange triangles same from Portenga et al. (2014).